Chromium doped copper vanadates photoanodes for water splitting

Drialys Cardenas-Morcoso, Anna Peiro-Franch, Isaac Herraiz-Cardona, Sixto Gimenez*

Institute of Advanced Materials (INAM), Universitat Jaume I, 12006 Castelló, Spain

***Corresponding author:** sjulia@uji.es

12 October 2016

Abstract

Solar hydrogen obtained from photoelectrochemical water splitting offers a versatile approach towards the substitution of fossil fuels by decentralized and sustainable resources, like water and sun. In the present study we have investigated the Chromium doped Copper Vanadate (Cr:$Cu_3V_2O_8$) as a candidate photoanode for photoelectrochemical water splitting. We have synthetized this material through a simple aqueous precipitation reaction, which easily allows compositional modifications. We have studied the effect of extrinsic doping with substitutional atoms like Chromium on the optical and photoelectrochemical properties. The main limiting factor for performance is related to the high bulk recombination, which is partially overcome by 0.75 at. % Chromium doping, with a five-fold enhancement of the charge separation efficiency at 1.23 V vs RHE. Despite this remarkable milestone, significant further improvement is needed for the technological exploitation of this material.

Keywords: water splitting, photoanode, copper vanadate, chromium doping

1. Introduction

The sun feeds the planet with an enormous amount of power, ~120 000 TW, that considerably exceeds the projected global energy demand for the next decades (~30 TW by 2050) in a moderate scenario.[1] Therefore, the conversion of sunlight into a profitable form of energy is almost mandatory to meet the needs of a growing world population with increasing living standards. Photoelectrochemical (PEC) water splitting offers an attractive technology for the conversion and storage of solar energy as chemical energy in the form of molecular bonds. In this process, the water molecule is decomposed into H_2 and O_2 under solar illumination. The O_2 evolution reaction (OER) is thermodynamically and kinetically more demanding, since four holes per molecule of produced oxygen are required. The strong oxidizing conditions needed for this reaction, severely limit the choice of adequate materials for viable operation. Consequently, the development of efficient and stable oxygen evolving photoanodes is one of the key challenges to success of this technology.[2, 3]

Since the pioneering study of Fujishima and Honda demonstrating UV light-assisted water splitting with TiO_2,[4] intensive research efforts have been carried out to find earth-abundant, efficient, stable and cost-effective materials that can absorb a significant fraction of the solar spectrum to split water. Metal oxides or oxo-metalates based on abundant materials, such as TiO_2,[4, 5] Fe_2O_3,[6] WO_3,[7] ZnO,[8] and $BiVO_4$,[9, 10] have been explored as candidate photoanode materials, satisfying both stability and cost requirements. Nevertheless, the low performance of these photoanodes attributed to poor electronic properties (Fe_2O_3 and $BiVO_4$) and/or large bandgaps (TiO_2, WO_3 and ZnO)[11] hinder their large-scale use in PEC systems. In order to overcome these problems, different strategies have been accomplished, involving combinatorial synthesis,[12] tuning the band structure of semiconductor materials by doping with different elements,[13, 14] surface

state passivation,[15, 16] surface activation with OER catalysts,[17, 18] and nanostructuring.[19-22]

At present, metal vanadates, mainly $BiVO_4$, are at the forefront of the research for PEC water splitting photoanodes.[13, 23, 24] A record photocurrent of 6.72 $mA \cdot cm^{-2}$ at 1.23 V vs RHE was obtained for $BiVO_4$, close to its theoretical maximum value (7.5 $mA \cdot cm^{-2}$), by means of combining nanostructuring with adequate OER catalysts.[25] Triclinic NiV_2O_6 films, fabricated by a vacuum deposition technique, have been recently tested for the first time as photoanodes for water oxidation. Although the observed photocurrent is relatively low (ca. 0.25 $mA \cdot cm^{-2}$ at 1.23 V vs RHE) according to the band gap (~2.4 eV) both the wide availability of the semiconductor components (Ni and V) and its stability in alkaline conditions postulate this material as a promising anode for PEC systems.[26]

Similar to NiV_2O_6, $Cu_3V_2O_8$ is an n-type semiconductor composed only of first-row transition metals. Although it has been previously examined for different applications (Li-ion batteries and degradation of organic pollutants),[27, 28] both, its bandgap near 2 eV and the adequate position of the valence band maximum make this material suitable for water photo-oxidation. To the best of our knowledge, there is only one recent study reporting the PEC performance of $Cu_3V_2O_8$ photoanodes. Seabold and Neale obtained a photocurrent of ca. 5 $\mu A \cdot cm^{-2}$ at 1 V vs RHE in 0.1 M potassium borate buffer at pH 9.2 for bare $Cu_3V_2O_8$ samples synthesized from the precipitation of nanoparticles of a simple hydroxide precursor. Also, it was found that doping with 0.75 at% Mo yielded an improvement of 40% in photocurrent, as a consequence of an increase in the electron diffusion length.[29] More recently, two different copper-based metal vanadates, i.e. CuV_2O_6 and $Cu_2V_2O_7$, were also reported as photoanodes for water splitting achieving photocurrent densities about 25 and 35 $\mu A \cdot cm^{-2}$, respectively, at 1.23 V vs RHE in 0.1 M sodium borate buffer solution.[30] In both studies, it was highlighted that the main

limitation of Cu-based vanadate materials for PEC performance is related to the low charge separation efficiency. On the other hand, vanadate compounds suffer from rapid corrosion due to the anodic dissolution of V species. Zhou et al. demonstrated that, in copper vanadate, the V corrosion is mitigated through a self-passivation process in which V corrodes from the film, leaving behind a Cu-rich oxide surface layer that prevents further V corrosion.[31] This investigation confirms that copper vanadate has indeed emerged as a promising photoanode for water splitting due to its stability, particularly in weakly alkaline borate electrolytes.

In the present work, we report our efforts aiming at improving the charge transport and charge separation efficiency of this semiconductor material. We have employed a synthetic method inspired on that previously reported.[29] This material was doped with chromium (Cr: $Cu_3V_2O_8$), which has an atomic radii of 0.74 Å, close to that of Cu^{2+} (0.73 Å), making feasible the exchange of both atoms in the CuO_6 octahedra of its crystalline structure, enhancing the extrinsic n-type doping of the semiconductor oxide. A detailed optoelectronic and photoelectrochemical characterization has been performed to quantitatively assess the contribution of the three fundamental processes involved in PEC, i.e. charge carrier generation, charge transport to the semiconductor-liquid interface and interfacial charge transfer, to the obtained photocurrent.

2. Materials and methods

2.1. Materials and synthesis

Preparation of nanoparticles of $Cu_3V_2O_7(OH)_2 \cdot 2H_2O$ was carried out following the procedure described in reference [29], with slight modifications, using as reagents: NH_4VO_3 (ASC reagent, ≥99.0%, Sigma-Aldrich) and $Cu(CH_3COO)_2 \cdot H_2O$ (puriss. p.a. ≥99.0%, Sigma-Aldrich). According to this, an initial $Cu_3V_2O_7(OH)_2 \cdot 2H_2O$ nanoparticles

suspension was prepared by a simple precipitation reaction synthesis. The precursor was recovered by successive centrifugation at 4000 rpm for 6 min and washing with absolute ethanol and finally re-suspended in 20 mL of ethanol. From this solution, a fraction was taken and diluted to obtain a 0.22 M copper content solution. Also, a drop of Triton X-100 was added in order to enhance the homogeneity of the deposition. Cr:$Cu_3V_2O_7(OH)_2{\cdot}2H_2O$ nanoparticles were prepared by adding the required amount of 0.22 M $CrCl_3{\cdot}6H_2O$ (p.a. ≥98%) solution into 10.0 mL of $Cu_3V_2O_7(OH)_2{\cdot}2H_2O$ suspension in order to obtain the desired Cr:Cu ratio (e.g. 75 μL of $CrCl_3{\cdot}6H_2O$ for 0.75% of Cr content).

Fluorine doped tin oxide (FTO) coated glass electrodes of 3.0 x 1.0 cm^2 area were washed by successive ultra-sonication for 15 min in soap (Hellmanex), Milli-Q water, ethanol, acetone and isopropanol and dried with compressed air. Before the deposition of the nanoparticles, the FTO substrates were treated in a UV−O_3 chamber for 15 min. Films of different thickness were prepared by spin coating a different number of layers of the $Cu_3V_2O_7(OH)_2{\cdot}2H_2O$ precursor on the FTO glass. Spin coating was carried out at 3000 rpm for 30 s, using 40 μL of precursor for each deposited layer. These films were dried on a hot plate preheated to 200 °C for 2 min and then annealed at 425°C for 1 h, preceded by a 2 h ramp up to obtain dark orange oxide films.

2.2 Structural, optical and photoelectrochemical characterizations

X-ray diffraction (XRD) data were obtained employing Cu Kα radiation at room temperature, scanning the samples from 10º to 70º (2θ) with a step of 0.02º. The morphology and thickness of both the precursor and oxide films were determined by scanning electron microscopy (SEM) using a JEOL JEM-3100F field emission scanning electron microscope. UV-Vis absorption spectra were recovered with a Cary 300 UV−Vis Varian spectrophotometer, between 300 and 800 nm. The absorbance (A) was estimated from transmittance (T) and diffuse reflectance (R) measurements as: $A =$

$-\log(T+R)$. The indirect optical bandgap was estimated by the Tauc plot as: $(h\upsilon\alpha)^{1/n} = A(h\upsilon - E_g)$. In this expression, the absorption coefficient (α) was calculated by $A = \alpha l$, where l is the thickness of the electrode.

Photoelectrochemical (PEC) measurements were performed using a PGSTAT302N potentiostat from AutoLab in a three-electrode configuration, with a Pt wire as counter electrode and Ag/AgCl, KCl (3M) as reference electrode, in a buffer of 0.1 M H_3BO_3 (≥99.8%, Riedel-deHäen) adjusted to pH 9.2 using KOH. In some cases, a fraction of 0.1 M Na_2SO_3 (≥98%, Sigma-Aldrich) was added to the borate buffer as sacrificial hole scavenger to suppress undesirable surface recombination reactions[32, 33] and increase the hole transfer kinetics at the semiconductor/liquid interface. The scan rate for cyclic voltammetry measurements was 50 mV s^{-1}. Photocurrent measurements were recorded under AM1.5 100 mW/cm^2 using a Xe lamp previously calibrated with an NREL-calibrated Si solar cell. In all cases, reported potential (E) was referred to the reversible hydrogen electrode (RHE) through the Nernst equation: $E_{RHE} = E_{Ag/AgCl} + 0.059\,V \times pH$. The same experimental setup was employed for chronoamperometric measurements, which were performed at 1.23 V vs RHE for 1h. For impedance spectroscopy (IS), a 20 mV amplitude sinusoidal perturbation at frequencies between 0.01 Hz and 1 MHz was used. Mott–Schottky analysis was performed in the dark at different frequencies (10 Hz, 50 Hz and 100 Hz). Incident photon-to-current efficiency (ICPE) was measured by employing a 300 W Xe lamp coupled to a monochromator. The photoelectrode was polarized at the desired voltage and the photocurrent was measured using an optical power meter 70 310 from Oriel Instruments. A Si photodiode was used to measure the light intensity to calibrate the system. IPCE was calculated with the expression: $IPCE\,\% = \frac{I_{ph}(A)}{P(W)} \times \frac{1239.8}{\lambda\,(nm)} \times 100$.

3. Results and discussion

In order to optimize both the homogeneity and reproducibility for the preparation of the oxide films, the deposition of the precursor solution was rigorously controlled. In first place, the synthesis of the precursor by a precipitation reaction provided a very easy and versatile way to control both the doping density and the concentration of nanoparticles in the precursor solution. On the other hand, spin coating proved to be the most reproducible method to obtain different film thicknesses by controlling the number of deposited layers of the same volume and concentration. Film thicknesses of 400 nm, 600 nm and 800 nm were obtained for 2, 3 and 4 deposited layers, respectively, for the precursor and final oxide films (see Supplementary Information, Fig. SI1). Deposition of more than four layers of precursor resulted in inhomogeneous films. The crystalline structure of the $Cu_3V_2O_7(OH)_2 \cdot 2H_2O$ precursor was confirmed by XRD analysis, (Fig. 1). The crystalline system is monoclinic with space group C2/m, and no secondary phases were observed. The structure of the final oxides was also confirmed as monoclinic (space group P21/c) in good agreement with the reference pattern. The effect of the incorporation of chromium on the crystalline structure was also studied. No representative changes due to the presence of new phases or different peak intensity ratios were detected. However, a slight shift of the [012] peak position (2θ=32.2º) with the increase in chromium content is noted, particularly at the highest Cr concentration (1.5%), as depicted in Fig. 1. These shifts are directly related to the interplanar distance through the Bragg´s equation $2d_{hkl}sen\theta_{hkl}=n\lambda$, demonstrating the incorporation of chromium in the crystalline lattice.

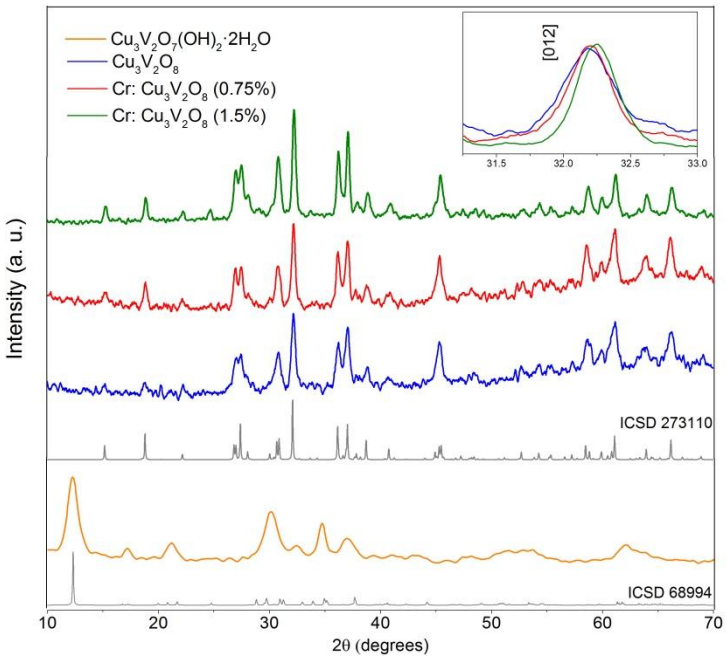

Fig. 1. XRD spectra of $Cu_3V_2O_7(OH)_2 \cdot 2H_2O$, $Cu_3V_2O_8$ and Cr:$Cu_3V_2O_8$ powders. The reference patterns for these phases are also included: ICSD 68994 for $Cu_3V_2O_7(OH)_2 \cdot 2H_2O$ precursor and ICSD 273110 for $Cu_3V_2O_8$. The inset graph shows an amplification of the maximum corresponding to the [012] direction to clearly illustrate the 2θ shift with Cr doping.

The morphology and particle size was determined by SEM (Fig. 2). The films of the precursor were composed of nanoflakes with around 70-80 nm size (Fig. 2a). In contrast, after annealing, both undoped and Cr-doped nanoparticles showed a globular morphology (Fig. 2b and c), with lower particle size for the doped nanoparticles (approximately 40-100 nm vs 20-80 nm, respectively) at the optimum Cr concentration (0.75%).

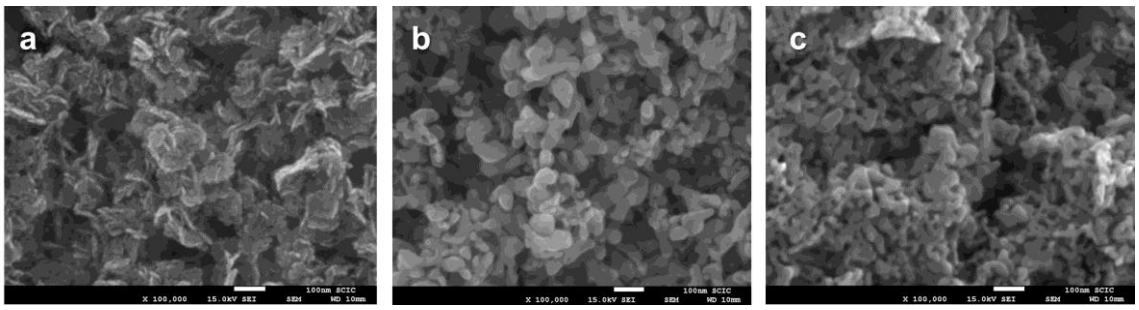

Fig. 2. Top-view micrographs of $Cu_3V_2O_7(OH)_2 \cdot 2H_2O$ (a), $Cu_3V_2O_8$ (b), and Cr:$Cu_3V_2O_8$ (0.75%) (c) obtained by SEM. Film thickness: 800 nm

The optical properties of the $Cu_3V_2O_8$ films with different thickness values are summarized in Fig. 3a. The absorbance increases monotonically with film thickness as expected, and the films can absorb light up to approximately 600 nm. Fig. 3b shows the effect of Cr doping on the optical properties, clearly indicating that the optical response of the $Cu_3V_2O_8$ films are not significantly modified after doping (Fig. SI2 illustrates this effect for all thickness values). The inset in Fig. 3b shows the Tauc plot for indirect transitions, and the calculated indirect bandgap for both undoped and doped $Cu_3V_2O_8$ films (2.0 eV) is in excellent agreement with that previously reported.[29]

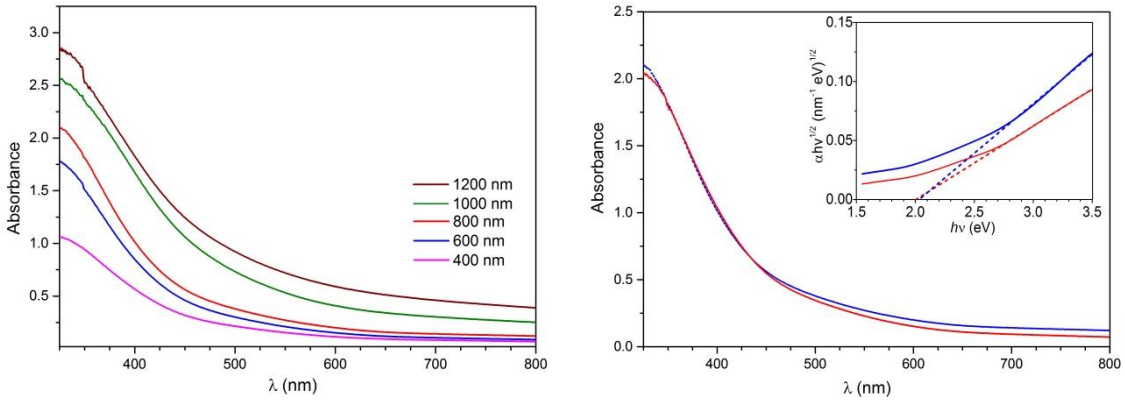

(a) (b)

Fig. 3. (a) Absorbance of $Cu_3V_2O_8$ with different thickness values. (b) Absorbance spectra of $Cu_3V_2O_8$ (blue) and Cr:$Cu_3V_2O_8$ (0.75%) (red) films of 800 nm thickness. Inset: Tauc plots for the determination of the indirect bandgap transition (2.0 eV).

In order to evaluate both the optimum thickness and Cr concentration of the films, the functional performance as oxygen evolving photoanodes was characterized by the j-V curves of doped and undoped $Cu_3V_2O_8$ photoanodes in the dark and under illumination at 100 $mW \cdot cm^{-2}$ in a borate buffer solution (pH 9.2), as compiled in Fig. 4. Fig. 4.a shows that the 800 nm thick samples yield the best performance, which can be attributed to the

inhomogeneous material distribution as the number of spin coating cycles increases. With respect to the Cr content, the optimum doping concentration appears at 0.75%, which means a three-fold enhancement at 1.5 V vs RHE compared to pristine $Cu_3V_2O_8$ (Fig. 4b). Dopant concentrations higher than 0.75% (i.e. 1% and 1.5%) did not improve the obtained photocurrent, as showed in the inset on Fig. 4b.

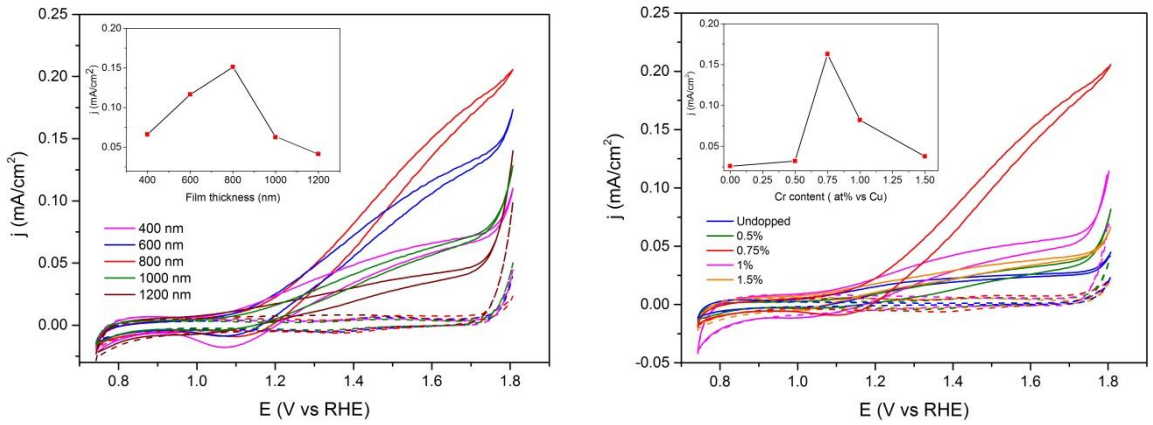

Fig. 4. j-V curves of undoped and Cr-doped $Cu_3V_2O_8$ films in borate buffer at pH 9.2 in the dark (dashed lines) and under front-side illumination at 100 $mW \cdot cm^{-2}$ (dashed lines). (a) Effect of thickness (0.75% Cr content). (b) Effect of Cr loading (800 nm thickness). Insets in (a) and (b) indicate the photocurrent at 1.54 V for different film thickness and Cr concentration, respectively.

Fig. 5a and b show the j-V curves for the optimum Cr concentration and film thickness in borate buffer at pH 9.2 in the dark and under front illumination with and without a hole scavenger (0.1 M Na_2SO_3) added to the solution, respectively. This sacrificial agent was employed to minimize the surface limitations of the material. The obtained photocurrent for sulfite oxidation is increased from 66 to 100 $\mu A \cdot cm^{-2}$ at 1.0 V vs RHE due to the Cr-doping. The enhancement reported again for the Cr:$Cu_3V_2O_8$ film indicates that, as a result of the doping process, there is not a significant improvement in the surface catalytic

properties of the photoanode, as also illustrated by the similar charge injection yield obtained for both undoped and Cr doped materials (Fig. 6b).

The spectral signature of the photocurrent was characterized by incident photon to current conversion efficiency (IPCE) for both undoped and Cr-doped films without and with the addition of the hole scavenger (Fig. 5). Insets in this Fig. display the magnification of the onset region, showing a good correspondence between the onset wavelength for the IPCE and the absorbance of the films (Fig. 3), around 600 nm. There is also an excellent agreement between the integrated photocurrent extracted from the IPCE spectra and that obtained from the j-V measurements (Fig. 5c and d), as illustrated in Supplementary Information, Table SI1.

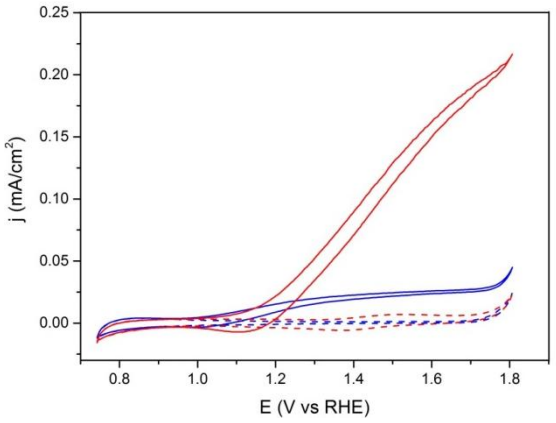

(a)

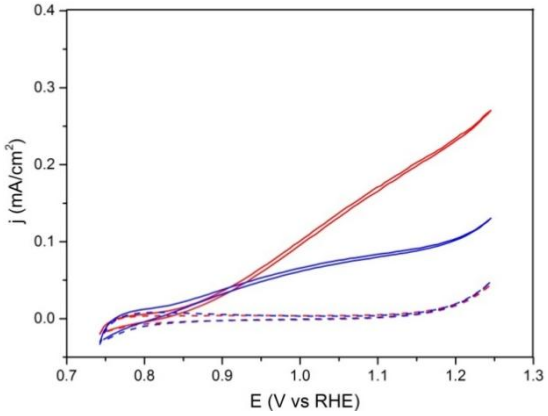

(b)

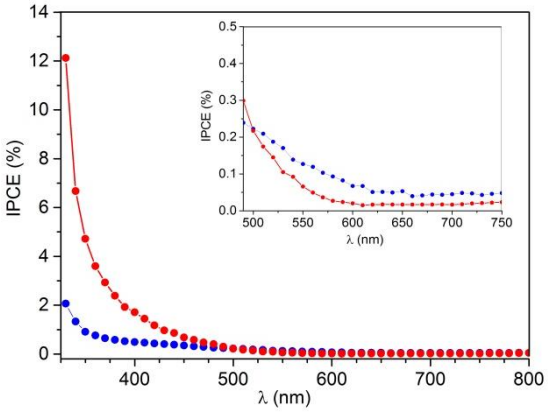

(c)

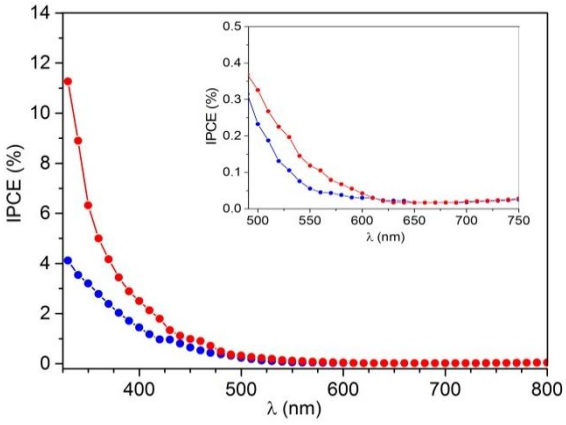

(d)

Fig. 5. j-V curves of 800 nm $Cu_3V_2O_8$ (blue lines) and Cr: $Cu_3V_2O_8$ (red lines) films obtained in the dark (dashed lines) and under front-side illumination at 100 mW·cm^{-2} (solid lines) in borate buffer at pH 9.2 (a) without and (b) with hole scavenger (0.1 M Na_2SO_3). IPCE spectra of 800 nm undoped $Cu_3V_2O_8$ (blue symbols) and Cr:$Cu_3V_2O_8$ (red symbols) films obtained in borate buffer at pH 9.2 (c) at 1.54 V vs RHE without hole scavenger and (d) at 1.0 V vs RHE with hole scavenger (0.1 M Na_2SO_3). The inset plots show a magnification of the onset region.

In order to quantitatively evaluate the limiting factors for performance of the synthesized materials, the two critical parameters i.e. the charge separation (η_{cs}) and charge injection (η_{cat}) yields were calculated for both doped and undoped oxide. In principle, the maximum photocurrent density that can be obtained if all the electron-hole pairs take part in the OER, j_{abs}, can be calculated from the optical measurements by integrating the solar photon flux (Φ_λ [photons/(m^{2}s)]), from the lower limit of the measured solar spectrum to the absorption edge (600 nm) of the oxide: $j_{abs} = \int(\Phi_\lambda \times q)d\lambda$. The calculated theoretical photocurrent was 12.90 mA·cm^{-2} and 11.21 mA·cm^{-2} for 800 nm thick undoped and Cr doped films, respectively. In aqueous electrolyte, the photocurrent density (j_{H_2O}) could be affected mainly by the charge separation efficiency on the bulk material and the charge injection efficiency related with the surface kinetic reaction or catalytic efficiency [33], so that: $j_{H_2O} = j_{abs} \times \eta_{cs} \times \eta_{cat}$. In presence of the hole scavenger, we assume that the catalytic efficiency is close to unity, so the obtained photocurrent density (j_{HS}) will be affected only by the charge separation efficiency: $j_{HS} = j_{abs} \times \eta_{cs}$.

The comparative behavior of both calculated yields is showed in Fig. 6. The low η_{cs} values (< 2%) obtained for the undoped material highlight the excessive bulk recombination losses in this material, which constitute the main limiting factor for performance. Chromium doping significantly increases η_{cs}, (with a five-fold enhancement

at 1.23 V vs RHE), although the obtained values are still low for further technological deployment of this material. On the other hand, the effect of chromium doping on η_{cat} is negligible. The addition of water oxidation co-catalysts could significantly enhance this yield, although given the high bulk recombination losses reflected in the low η_{cs} yields, further efforts towards improving the catalytic performance of this material were not attempted. It is important to highlight that the method employed to calculate η_{cs} and η_{cat} based on the use of a hole scavenger does not differentiate between improved catalysis and reduced surface recombination, which is a limitation for a more robust assessment. In any case, it provides a clear difference between bulk and surface origin of the enhanced performance and in the present study it clearly helps to understand that main origin of the enhancement produced by Cr doping arises from the bulk properties of the material.

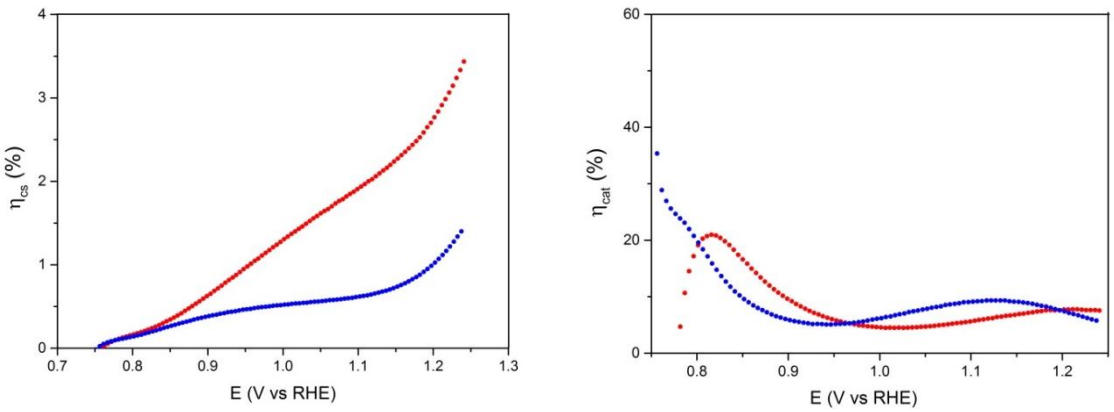

(a) (b)

Fig. 6. (a) Charge separation efficiency (η_{cs}) and (b) Charge injection efficiency (η_{cat}) for 800 nm films of $Cu_3V_2O_8$ (blue) and Cr:$Cu_3V_2O_8$ (red).

Impedance spectroscopy (IS) measurements were carried out to assess the electronic properties of the $Cu_3V_2O_8$ photoanodes, i.e., doping density (N_D) and flatband potential (V_{fb}), by means of Mott-Schottky (MS) plots. The value for the relative dielectric permittivity (ε) was estimated as 44.[34] This study was performed in dark conditions covering a wide potential window (from 0.5 to 1.5 V vs RHE) and at single frequencies (10

Hz, 50 Hz and 100 Hz, respectively). The frequencies were selected from the region at which the real part of the capacitance remained constant (10 Hz - 100 Hz) in preliminary multi-frequency tests (10 MHz - 100 mHz) at a constant applied bias (see Supplementary Information, Fig. SI5). Fig. 7 compares the MS plots obtained at a frequency of 10 Hz for doped and undoped $Cu_3V_2O_8$ films and with these plots, the values for N_D and V_{fb} were estimated. Note that identical MS plots were obtained for the measurements at 50 Hz and 100 Hz (see Supplementary Information, Fig. SI3). The lower slope reported for the Cr:$Cu_3V_2O_8$ samples with 0.75% and more significantly with 1% of chromiun content is connected to an increase in the doping density (Table 1) which can be attributed to the isomorphic replacement of Cu(II) by Cr(III) in the $Cu_3V_2O_8$ lattice, analogous to the V(V) substitution by Mo(VI) reported in other vanadates.[29, 35] The statistical significance of these results is illustrated in Supplementary Information, Fig. SI6, where four identical samples were measured at each condition. The flatband potential, V_{fb}, for $Cu_3V_2O_8$ photoanode is 0.79 V vs RHE, which is slightly more positive than the frequency-dependent values previously reported (between 0.63 and 0.69 V vs RHE) [29]. In addition, V_{fb} for the optimum Cr-doped film was around 120 mV cathodically shifted (0.67 V vs RHE), although this beneficial displacement is not reflected on the onset potential for the photocurrent, see Fig. 5a, probably due to the excessive bulk recombination losses. It is important to highlight that these very positive flatband potentials are detrimental for technological applications and further efforts should be conducted to shift cathodically this potential.

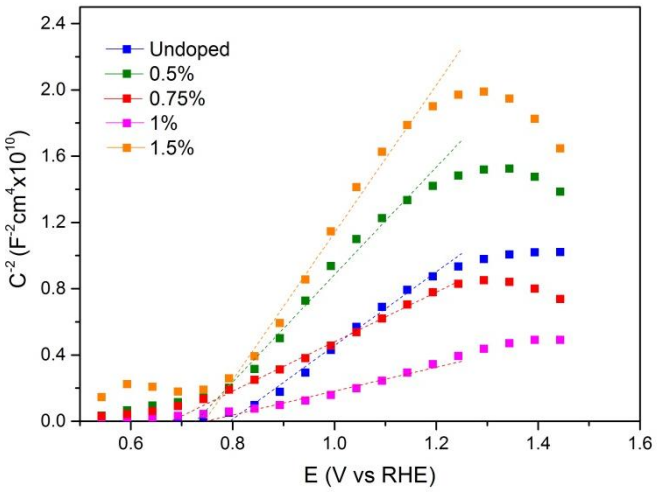

Fig. 7. Mott-Schottky plot of $Cu_3V_2O_8$ and Cr:$Cu_3V_2O_8$ films performed at 10 Hz in borate buffer at pH 9.2 and the lineal fitting showing the x-intercept corresponding to the flatband potential value, V_{fb}.

By substitutional Cr doping, replacing part of the Cu sites, the Fermi level of copper vanadate shifts towards the conduction band increasing the band bending at the semiconductor liquid junction and consequently enhancing charge separation (Fig. 6a). This has a beneficial effect on the photoelectrochemical performance. On the other hand, there is an anomaly on the donor density for 0.5% and 1.5% Cr additions. EDS and XPS experiments were carried out to understand the correlation between added Cr during the synthetic process and incorporated Cr into the specimens. Unfortunately the Cr contents employed are below the detection limit of these techniques and further information could not be obtained. XRD analysis did not show the presence of secondary phases at any Cr concentration tested, but a significant shift of the maximum on the [012] direction (Fig. 1) was registered at the highest concentration (1.5%), which could be related to a degradation of the film integrity as result of the strain induced by Cr replacing Cu positions into the periodic crystal lattice, with the consequent progressive decrease of the photocurrent showed in Fig. 4b for high Cr additions. In any case, further work is needed to understand the anomaly at the lowest Cr addition (0.5%). The morphological modification of the

electrodes with Cr addition, illustrated by Supplementary Information, Fig. SI7 could slightly affect the donor densities measured, but it is not believed to the main reason explaining the observed behavior.

Table 1. Estimated dopant density and flat band potential of $Cu_3V_2O_8$ and Cr:$Cu_3V_2O_8$ from the MS plots at 10 Hz.

	$Cu_3V_2O_8$	$Cr:Cu_3V_2O_8$			
		0.5%	*0.75%*	*1%*	*1.5%*
N_D ($10^{20}cm^{-3}$)	1.44	0.99	2.20	4.44	0.72
V_{fb} (V)	0.79	0.73	0.70	0.75	0.74

In order to evaluate the stability of these films, chronoamperometric measurements were performed at 1.23 V vs RHE for 1h (Fig. 8), finding a very stable behavior of photocurrent response, with an overall loss of around the 14 % at the end of the measurement with respect the five initial minutes for the measures with hole scavenger. The higher losses observed in the measurements performed in presence of the hole scavenger is related with the fact that the rapid removal of the photogenerated holes at the surface by the sulfite can compete with photocorrosion process, which was reported indeed in Mo-doped copper vanadates as well[29]. This remarks the fact that, for better performance of this material, an appropriated surface modification with a suitable oxygen reaction catalyst that can also avoid direct contact of the semiconductor surface with the electrolyte to prevent photocorrossion, is needed.

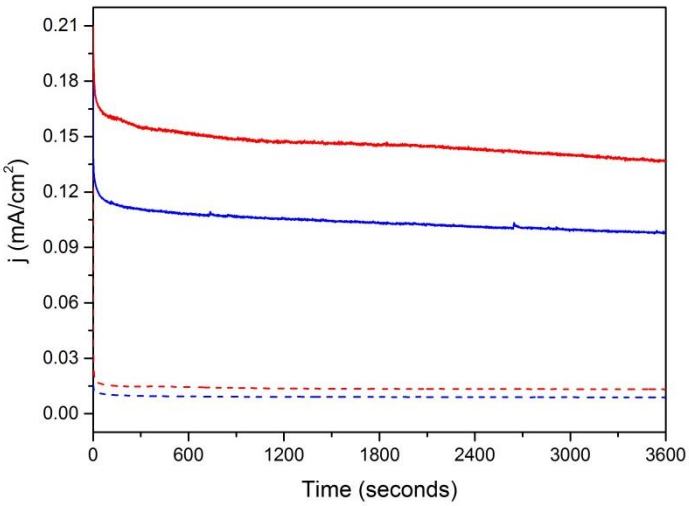

Fig. 8 Potentiostatic photocurrent of $Cu_3V_2O_8$ (blue) and Cr:$Cu_3V_2O_8$ (red) films at 1.23 V vs RHE in borate buffer at pH 9.2 without (dashed lines) and with 0.1 M Na_2SO_3 (solid lines).

Finally, in order to confirm that the obtained photocurrent actually stems from water oxidation, the O_2 evolution on Cr:$Cu_3V_2O_8$ (0.75 at. % of Cr content) electrodes was determined by performing chronoamperometric measurements at 1.54 V vs RHE under 1 sun illumination in a sealed cell, and the output gas flow was analyzed by chromatography. From the chronoamperometric measurement the theoretical O_2 production was estimated through the Faraday´s law, as represented in Fig. 9a (black line) and compared with the measured values (red symbols). Because of the dispersion on the obtained values, related with imperfections on the manual sampling during the chromatography analysis, a linear fitting is represented for a better comparison. The measured O_2 produced in this photoanode correlate well with respect the theoretical estimated, being the faradic efficiency > 90% after 1h, as is represented in Fig. 9b. The fact that there is not reached a 100% of faradic efficiency must likely related with photocorrosion process of the semiconductor in contact with the electrolyte, which have been also observed in $BiVO_4$-based photoanodes, were the faradic efficiency losses have been related with imperfect coverage of the semiconductor surface by the catalyst material[36] , which remarks the

need to employ this kind of strategies in further investigations in order to improve the photocatalytic feature of this semiconductor and achieve competitive efficiency performance.

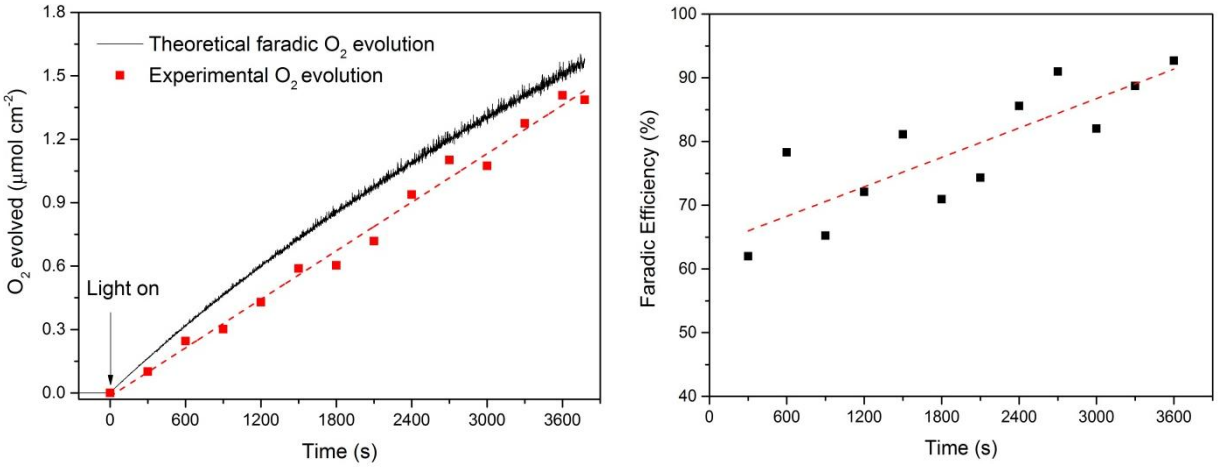

(a) (b)

Fig. 9. (a) Oxygen evolution in borate buffer at pH 9.2 measured under continuous 1 sun irradiation at 1.54 V versus RHE registered experimentally by gas chromatography (red squares) and theoretically calculated from the measured current by the Faraday's law (black line). (b) Faradic efficiency obtained from comparing the theoretical and experimental oxygen evolution showed in (a).

4. Conclusions

In summary, we have studied the optical and photoelectrochemical properties of $Cu_3V_2O_8$ as a candidate photoanode for photoelectrochemical water splitting and explored the effect of Cr doping aiming at overcoming the large bulk recombination losses in this material. Our results show that although a remarkable improvement is photocurrent is obtained after 0.75 at.% Cr doping, which can be related to an increased extrinsic doping of the material, further efforts must be carried out in order to achieve competitive charge separation yields (>70%) for technological deployment. Additionally, the flatband should

be shifted to more cathodic potentials to allow the exploration of alternative configurations based on n-n heterojunctions.

Acknowledgements

We thank financial support from the University Jaume I through the project P1·1B2011-50 and from the Generalitat Valenciana, through the project PROMETEOII/2014/020 and the Santiago Grisolia Program, grant 2015-031. Serveis Centrals at UJI (SCIC) are also acknowledged.

References

[1] P.V. Kamat, Meeting the Clean Energy Demand: Nanostructure Architectures for Solar Energy Conversion, The Journal of Physical Chemistry C 111 (2007) 2834-2860.

[2] K. Sivula, Metal Oxide Photoelectrodes for Solar Fuel Production, Surface Traps, and Catalysis, The Journal of Physical Chemistry Letters 4 (2013) 1624-1633.

[3] S. Cho, J.-W. Jang, K.-H. Lee, J.S. Lee, Research Update: Strategies for efficient photoelectrochemical water splitting using metal oxide photoanodes, APL Mater. 2 (2014) 010703.

[4] A. Fujishima, K. Honda, Electrochemical Photolysis of Water at a Semiconductor Electrode, Nature 238 (1972) 37-38.

[5] J. Nowotny, T. Bak, M.K. Nowotny, L.R. Sheppard, Titanium dioxide for solar-hydrogen I. Functional properties, International Journal of Hydrogen Energy 32 (2007) 2609-2629.

[6] K. Sivula, F. LeFormal, M. Grätzel, Solar Water Splitting: Progress Using Hematite (α-Fe_2O_3) Photoelectrodes, ChemSusChem 4 (2011) 432-449.

[7] M.A. Butler, Photoelectrolysis and physical properties of the semiconducting electrode WO_2 Journal of Applied Physics 48 (1977) 1914-1920.

[8] A. Wolcott, W.A. Smith, T.R. Kuykendall, Y. Zhao, J.Z. Zhang, Photoelectrochemical Study of Nanostructured ZnO Thin Films for Hydrogen Generation from Water Splitting, Advanced Functional Materials 19 (2009) 1849-1856.

[9] A. Kudo, K. Omori, H. Kato, A novel aqueous process for preparation of crystal form-controlled and highly crystalline $BiVO_4$ powder from layered vanadates at room temperature and its photocatalytic and photophysical properties, Journal of the American Chemical Society 121 (1999) 11459-11467.

[10] K. Sayama, A. Nomura, Z. Zou, R. Abe, Y. Abe, H. Arakawa, Photoelectrochemical decomposition of water on nanocrystalline $BiVO_4$ film electrodes under visible light, Chemical Communications (2003) 2908-2909.

[11] C. Santato, M. Ulmann, J. Augustynski, Photoelectrochemical Properties of Nanostructured Tungsten Trioxide Films, The Journal of Physical Chemistry B 105 (2001) 936-940.

[12] M. Woodhouse, B.A. Parkinson, Combinatorial approaches for the identification and optimization of oxide semiconductors for efficient solar photoelectrolysis, Chemical Society Reviews 38 (2009) 197-210.
[13] F.F. Abdi, L. Han, A.H.M. Smets, M. Zeman, B. Dam, R. van de Krol, Efficient solar water splitting by enhanced charge separation in a bismuth vanadate-silicon tandem photoelectrode, Nature Communications 4 (2013).
[14] L. Steier, I. Herraiz-Cardona, S. Gimenez, F. Fabregat-Santiago, J. Bisquert, S.D. Tilley, M. Graetzel, Understanding the Role of Underlayers and Overlayers in Thin Film Hematite Photoanodes, Advanced Functional Materials 24 (2014) 7681-7688.
[15] C. Du, X. Yang, M.T. Mayer, H. Hoyt, J. Xie, G. McMahon, G. Bischoping, D. Wang, Hematite-Based Water Splitting with Low Turn-On Voltages, Angewandte Chemie-International Edition 52 (2013) 12692-12695.
[16] O. Zandi, T.W. Hamann, Enhanced Water Splitting Efficiency Through Selective Surface State Removal, Journal of Physical Chemistry Letters 5 (2014) 1522-1526.
[17] T.W. Kim, K.-S. Choi, Nanoporous $BiVO_4$ Photoanodes with Dual-Layer Oxygen Evolution Catalysts for Solar Water Splitting, Science 343 (2014) 990-994.
[18] J. Suntivich, K.J. May, H.A. Gasteiger, J.B. Goodenough, Y. Shao-Horn, A Perovskite Oxide Optimized for Oxygen Evolution Catalysis from Molecular Orbital Principles, Science 334 (2011) 1383-1385.
[19] Y. Pihosh, I. Turkevych, K. Mawatari, T. Asai, T. Hisatomi, J. Uemura, M. Tosa, K. Shimamura, J. Kubota, K. Domen, T. Kitamori, Nanostructured $WO_3/BiVO_4$ Photoanodes for Efficient Photoelectrochemical Water Splitting, Small 10 (2014) 3692-3699.
[20] I. Cesar, A. Kay, J.A.G. Martinez, M. Gratzel, Translucent thin film Fe_2O_3 photoanodes for efficient water splitting by sunlight: Nanostructure-directing effect of Si-doping, Journal of the American Chemical Society 128 (2006) 4582-4583.
[21] F.E. Osterloh, Inorganic nanostructures for photoelectrochemical and photocatalytic water splitting, Chemical Society Reviews 42 (2013) 2294-2320.
[22] Y. Lin, S. Zhou, S.W. Sheehan, D. Wang, Nanonet-Based Hematite Heteronanostructures for Efficient Solar Water Splitting, Journal of the American Chemical Society 133 (2011) 2398-2401.
[23] X. Shi, Y. Choi, K. Zhang, J. Kwon, D.Y. Kim, J.K. Lee, S.H. Oh, J.K. Kim, J.H. Park, Efficient photoelectrochemical hydrogen production from bismuth vanadate-decorated tungsten trioxide helix nanostructures, Nature Communications 5 (2014).
[24] X. Shi, K. Zhang, K. Shin, M. Ma, J. Kwon, I.T. Choi, J.K. Kim, H.K. Kim, D.H. Wang, J.H. Park, Unassisted photoelectrochemical water splitting beyond 5.7% solar-to-hydrogen conversion efficiency by a wireless monolithic photoanode/dye-sensitised solar cell tandem device, Nano Energy 13 (2015) 182-191.
[25] Y. Pihosh, I. Turkevych, K. Mawatari, J. Uemura, Y. Kazoe, S. Kosar, K. Makita, T. Sugaya, T. Matsui, D. Fujita, M. Tosa, M. Kondo, T. Kitamori, Photocatalytic generation of hydrogen by core-shell $WO_3/BiVO_4$ nanorods with ultimate water splitting efficiency, Scientific Reports 5 (2015) 11141.

[26] H.X. Dang, A.J.E. Rettie, C.B. Mullins, Visible-Light-Active NiV_2O_6 Films for Photoelectrochemical Water Oxidation, The Journal of Physical Chemistry C 119 (2015) 14524-14531.
[27] S. Zhang, Y. Sun, C. Li, L. Ci, $Cu_3V_2O_8$ hollow spheres in photocatalysis and primary lithium batteries, Solid State Sciences 25 (2013) 15-21.
[28] J. Dai, M. Lai, R.M. LaFollette, D. Reisner, Thin Film Copper Vanadium Oxide Electrodes for Thermal Batteries, ECS Transactions 33 (2011) 3-9.
[29] J.A. Seabold, N.R. Neale, All First Row Transition Metal Oxide Photoanode for Water Splitting Based on $Cu_3V_2O_8$, Chemistry of Materials 27 (2015) 1005-1013.
[30] W. Guo, W.D. Chemelewski, O. Mabayoje, P. Xiao, Y. Zhang, C.B. Mullins, Synthesis and Characterization of CuV_2O_6 and $Cu_2V_2O_7$: Two Photoanode Candidates for Photoelectrochemical Water Oxidation, The Journal of Physical Chemistry C 119 (2015) 27220-27227.
[31] L. Zhou, Q. Yan, J. Yu, R.J.R. Jones, N. Becerra-Stasiewicz, S.K. Suram, A. Shinde, D. Guevarra, J.B. Neaton, K.A. Persson, J.M. Gregoire, Stability and self-passivation of copper vanadate photoanodes under chemical, electrochemical, and photoelectrochemical operation, Physical Chemistry Chemical Physics 18 (2016) 9349-9352.
[32] T. Hisatomi, J. Kubota, K. Domen, Recent advances in semiconductors for photocatalytic and photoelectrochemical water splitting, Chemical Society Reviews 43 (2014) 7520-7535.
[33] H. Dotan, K. Sivula, M. Graetzel, A. Rothschild, S.C. Warren, Probing the photoelectrochemical properties of hematite (α-Fe_2O_3) electrodes using hydrogen peroxide as a hole scavenger, Energy & Environmental Science 4 (2011) 958-964.
[34] S. Sarkar, K.K. Chattopadhyay, Size-dependent optical and dielectric properties of $BiVO_4$ nanocrystals, Physica E: Low-dimensional Systems and Nanostructures 44 (2012) 1742-1746.
[35] W.-J. Yin, S.-H. Wei, M.M. Al-Jassim, J. Turner, Y. Yan, Doping properties of monoclinic $BiVO_4$ studied by first-principles density-functional theory, Physical Review B 83 (2011) 155102.
[36] J.A. Seabold, K.-S. Choi, Efficient and Stable Photo-Oxidation of Water by a Bismuth Vanadate Photoanode Coupled with an Iron Oxyhydroxide Oxygen Evolution Catalyst, Journal of the American Chemical Society 134 (2012) 2186-2192.

Supplementary Information

Chromium doped copper vanadates photoanodes for water splitting

Drialys Cardenas-Morcoso, Anna Peiro-Franch, Isaac Herraiz-Cardona, Sixto Gimenez*

Institute of Advanced Materials (INAM), Universitat Jaume I, 12006 Castelló, Spain

Email: sjulia@uji.es

12 October 2016

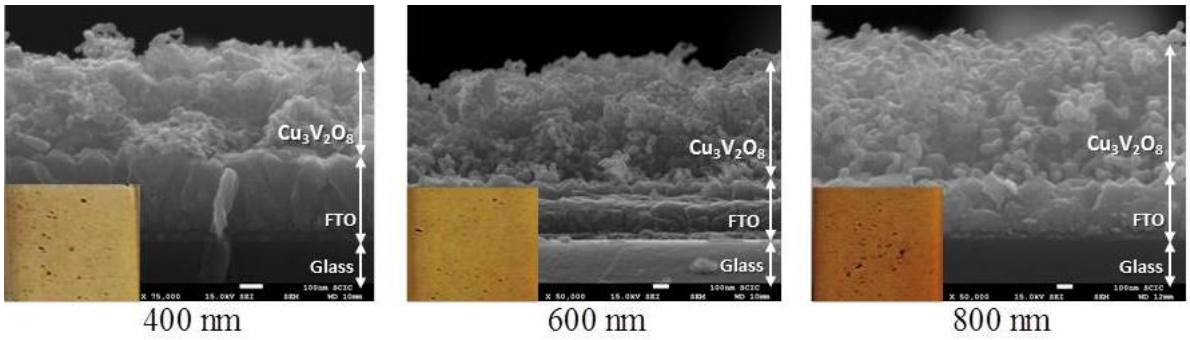

Figure SI1. Cross sections of the $Cu_3V_2O_8$ thin films after 425 ºC annealing with different thickness values as a result of the number of deposited layers during the spin coating. The scale bar is 100 nm in all micrographs.

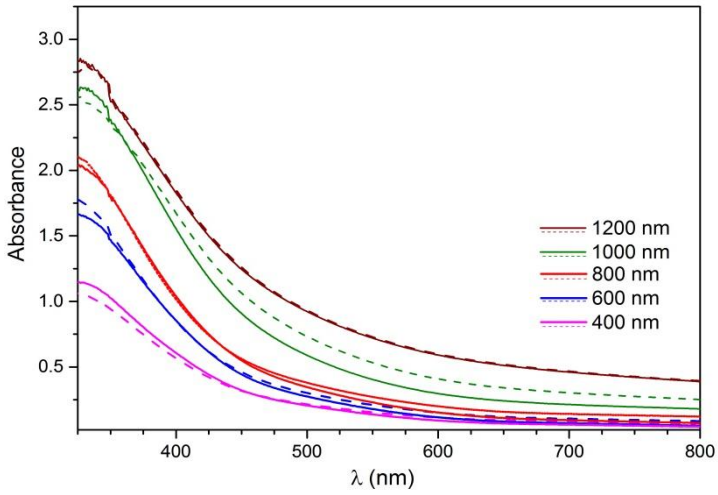

Figure SI2. Absorbance of $Cu_3V_2O_8$ (dashed lines) and Cr:$Cu_3V_2O_8$ (0.75%) (solid lines) with different thickness values.

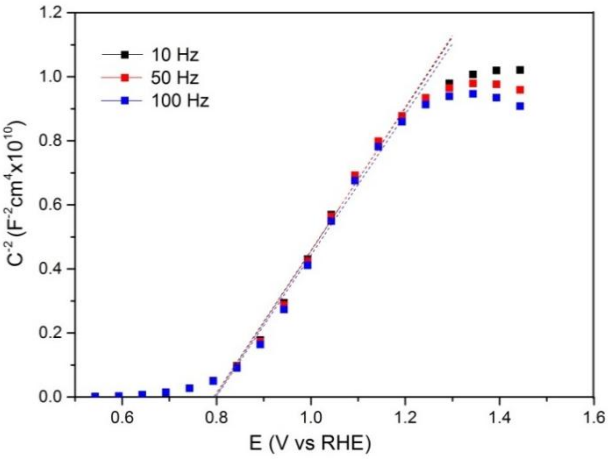

Figure SI3. Mott-Schottky plot of 600 nm $Cu_3V_2O_8$ films performed at 10 Hz, 50 Hz and 100 Hz in borate buffer at pH 9.2 and the corresponding lineal fitting showing the *x*-intercept.

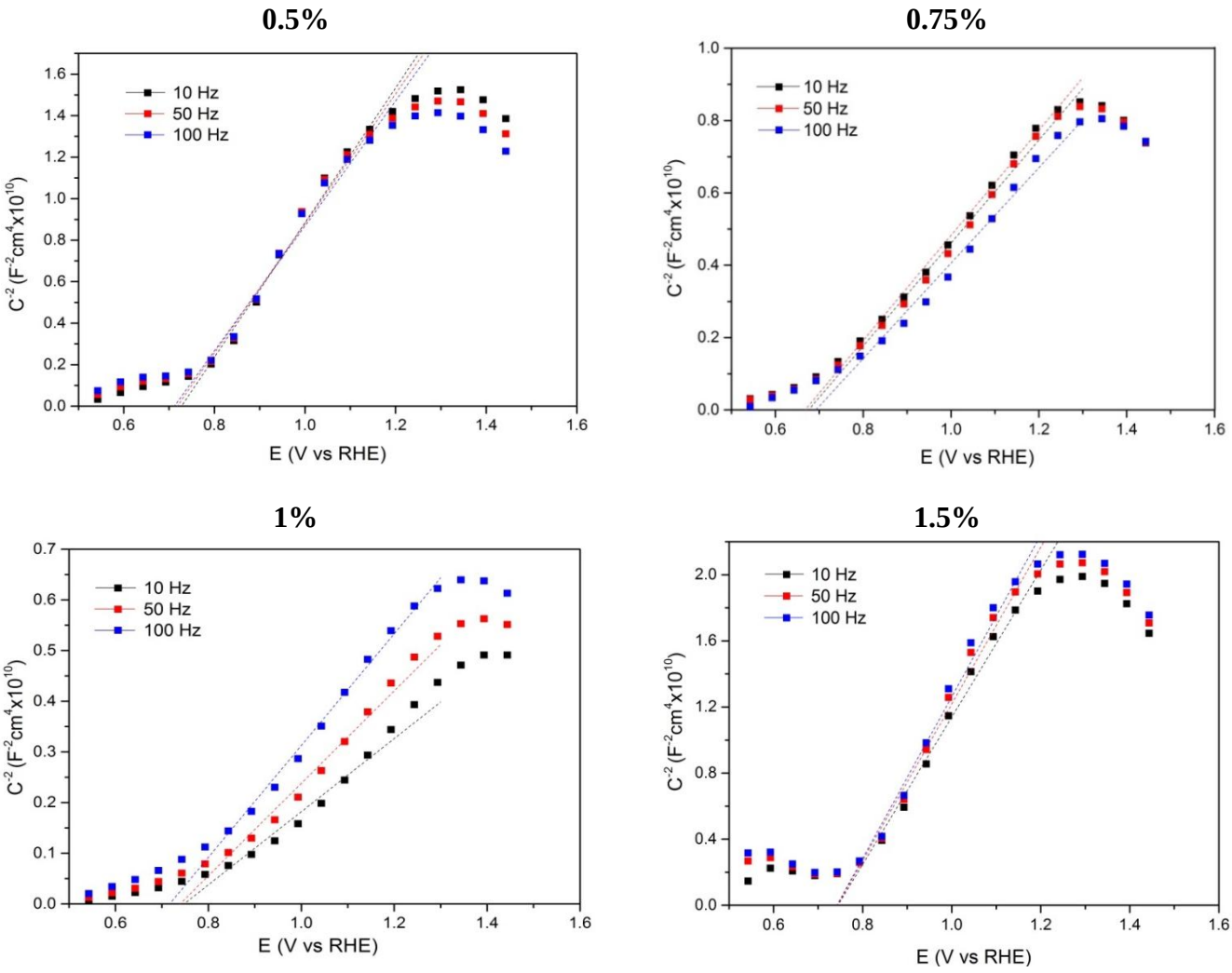

Figure SI4. Mott-Schottky plot of 600 nm Cr:$Cu_3V_2O_8$ films with different Cr vs Cu content performed at 10 Hz, 50 Hz and 100 Hz in borate buffer at pH 9.2 and the corresponding lineal fitting showing the *x*-intercept (flatband potential).

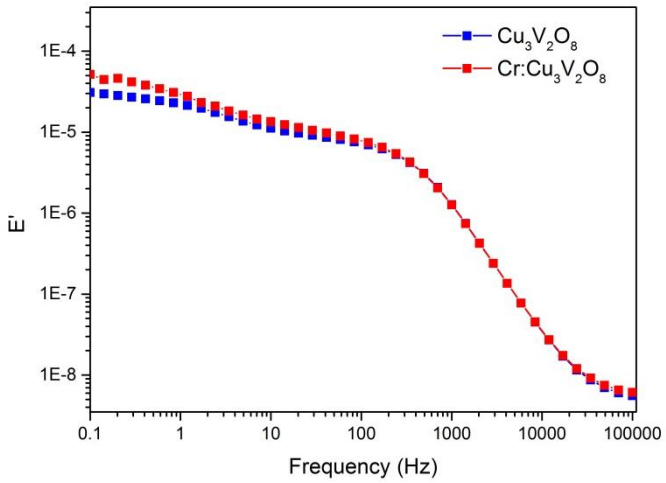

Figure SI5. Bode plots of the impedance spectra obtained in borate buffer at pH 9.2 and dark conditions, at 1.54 V vs RHE. The frequencies employed for Mott-Schottky analysis were selected from the region where the real part of the capacitance (E') remained constant (10-100 Hz).

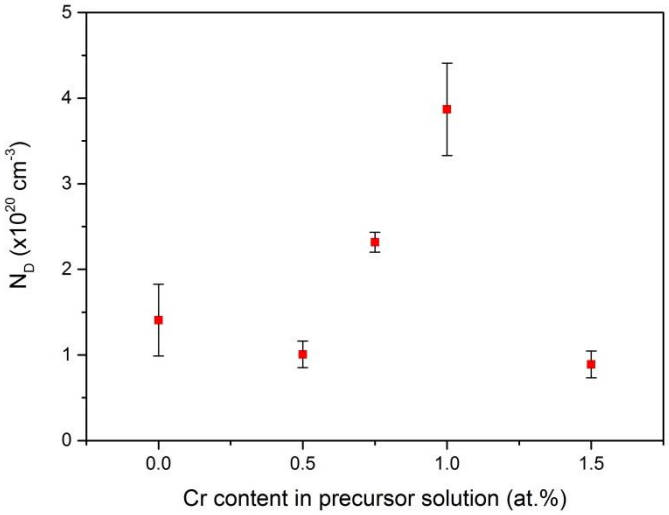

Figure SI6. N_D obtained as function of Cr content in the precursor solution. Four samples were tested at each condition and the error bars are indicated.

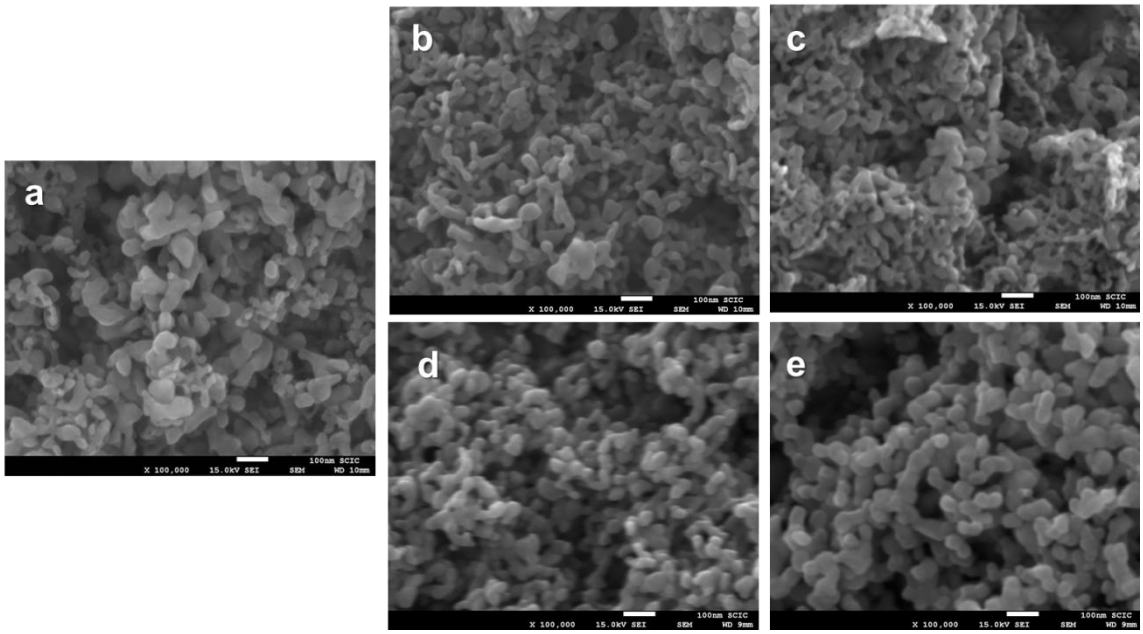

Figure SI7. Top-view of **a)** $Cu_3V_2O_8$, **b-e)** Cr: $Cu_3V_2O_8$ with 0.5%, 0.75%, 1% and 1.5% of Cr content in the precursor solution respectively, showing the effect of doping in the surface area. Scale bar is 100 nm in all micrographs.

Table SI1. Integrated currents from IPCE records compared with those obtained from the j-V curves. (Reported values are obtained at 1.54 V vs RHE and at 1 V vs RHE for water oxidation and hole scavenger oxidation, respectively).

	Integrated Current ($\mu A/cm^2$)	**Experimental Current ($\mu A/cm^2$)**
$Cu_3V_2O_8$	24	25
$Cu_3V_2O_8$ (in 0.1 M Na_2SO_3)	52	67
Cr:$Cu_3V_2O_8$	114	113
Cr:$Cu_3V_2O_8$ (in 0.1 M Na_2SO_3)	123	102